NANO LETTERS

Letter

pubs.acs.org/NanoLett

Architecturing Hierarchical Function Layers on Self-Assembled Viral Templates as 3D Nano-Array Electrodes for Integrated Li-Ion Microbatteries

Yihang Liu,[†] Wei Zhang,[‡] Yujie Zhu,[†] Yanting Luo,[†] Yunhua Xu,[†] Adam Brown,[§] James N. Culver,[§] Cynthia A. Lundgren,[∥] Kang Xu,*[,∥] Yuan Wang,[‡,*] and Chunsheng Wang*[,†]

[†]Department of Chemical and Biomolecular Engineering, University of Maryland, College Park, Maryland 20742, United States

[‡]Key Laboratory of Radiation Physics and Technology, Ministry of Education, Institute of Nuclear Science and Technology, Sichuan University, Chengdu 610064, People's Republic of China

[§]Institute for Bioscience and Biotechnology Research and Department of Plant Science and Landscape Architecture, University of Maryland, College Park, Maryland 20742, United States

[∥]Electrochemistry Branch, Power and Energy Division Sensor and Electron Devices Directorate, U.S. Army Research Laboratory, Adelphi, Maryland 20783, United States

Supporting Information

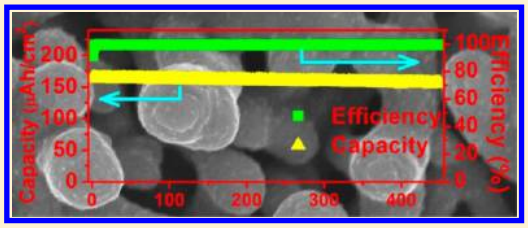

ABSTRACT: This work enables an elegant bottom-up solution to engineer 3D microbattery arrays as integral power sources for microelectronics. Thus, multilayers of functional materials were hierarchically architectured over tobacco mosaic virus (TMV) templates that were genetically modified to self-assemble in a vertical manner on current-collectors, so that optimum power and energy densities accompanied with excellent cycle-life could be achieved on a minimum footprint. The resultant microbattery based on self-aligned $LiFePO_4$ nanoforests of shell−core−shell structure, with precise arrangement of various auxiliary material layers including a central nanometric metal core as direct electronic pathway to current collector, delivers excellent energy density and stable cycling stability only rivaled by the best Li-ion batteries of conventional configurations, while providing rate performance per foot-print and on-site manufacturability unavailable from the latter. This approach could open a new avenue for microelectromechanical systems (MEMS) applications, which would significantly benefit from the concept that electrochemically active components be directly engineered and fabricated as an integral part of the integrated circuit (IC).

KEYWORDS: *3D microbattery arrays, nanohierarchy, tobacco mosaic virus, integral power for microelectronics, $LiFePO_4$ nanoforests, magnetron sputtering*

Since the birth of the Li-ion battery 2 decades ago, its energy/power density and cycling stability have been significantly advanced, thanks to both innovations in materials and optimization of cell engineering. This young battery chemistry in either prismatic or cylindrical configurations—both of 2D character—has dominated the multibillion dollar market of portable electronics as the rechargeable power source of choice, and is posing to prevail in more lucrative and strategically significant markets of automotive and stationary grid-storage applications. However, to a much lesser degree have these advances benefitted the on-board power needs of microelectronics, another fast-growing market of billion dollar scale, where amount of energy stored on given footprint (J/mm^2) precedes that in either unit weight (Wh/kg) or volume (Wh/L), and, more importantly, where the capability of battery active components being integrated as part of the integrated circuit (IC) during microfabrication process would prove a more superior advantage in manufacturability. Hence, in those micro/nanoelectromechanical systems (MEMS/NEMS) or biomedical devices, the desired on-board power delivery in exceptionally small geometric scales often meets the distinct challenge of accommodating the clumsy battery configurations of 2D nature that were originally designed for devices thousand or even million times larger in dimension. Furthermore, most conventional Li-ion battery key components (electrolytes, separators) cannot survive the integration process during the microfabrication process, characterized by the solder-reflow operation (260 °C). Even the solid thin film Li-ion batteries, although more amenable toward microfabrication process than liquid electrolyte Li-ion technology, are constrained by the Li melting point (180.6 °C), not to mention that their typical low power densities, mainly imposed by LiPON electrolyte and its limited reaction interface with electrodes, often fall short of the pulse demands of MEMS/NEMS devices. To address this shortcoming of thin film battery technology, Si−Li alloys have

Received: November 6, 2012
Revised: December 10, 2012
Published: December 19, 2012

been recently explored as an alternative anode for micro-batteries,[1] while various top-down processes familiar to the IC industry have been employed to design, assemble, and pack nanostructured electrode arrays.[2]

Approaching the challenge from a new avenue, the present work attempts to leverage a cathode technology, $LiFePO_4$, which has been matured by the Li-ion industry as a safe, low cost and high power density chemistry in conventional battery designs, as a potential active cathode for 3D nanoelectrode arrays. Bottom-up instead of top-down approaches were adopted, so that not only is on-site manufacturability complying to IC microfabrication allowed but also the usual challenge of high ionic/electronic resistance in nanometric scales could be readily resolved by precisely arranging multilayer of active and auxiliary materials over vertically assembled biotemplates, i.e., genetically modified clones of tobacco mosaic virus (TMV). The sophisticated micromechanism architectured in such manner stores and delivers energy at an excellent rate and efficiency as result of the synergistic collaboration of these various layers of materials.

Previously we have successfully used a similar but much simpler approach to fabricate a self-aligned 3D Si nanoanode arrays.[3] The coupling of these anode and cathode chemistries enabled by the current bottom-up nanohierarchical technique would eventually pave the way to fabricate an all-solid-state 3D $LiFePO_4$/LiPON/Si nanoforests microbattery.

The primary challenge encountered by a 2D-nature electrode in MEMS configuration is the limited footprint (usually in μm^2). To maximize the active sites for energy storage per geometric area, one will be forced to seek space in the third dimension, leading to investigations of 3D design for microelectrode arrays.[2] A logic development of this approach leads to the architecture of rod-like structures that would stand vertically on the substrates while loading active components with its much heightened surface area. Recent advances in nanomaterial engineering have enabled diversified routes to such nanorod preparations, and an increasingly number of mature cathode chemistries from the conventional Li-ion industry has been applied. However, an intrinsic challenge stemming from the high aspect ratio of rod-like structures would be the new kinetic control for the intrinsically poor electronic conductor $LiFePO_4$, which affects the rate of power delivery. Although the increased electrolyte/electrode contacts in these 3D electrode designs significantly facilitates "ionic transfer" by reducing tortuosity in migration pathway, the electron transfer between the current collector and $LiFePO_4$ active species, on the other hand, has to occur through a longer pathway along the elongated shape of the $LiFePO_4$ rods, which is hampered by the usually very high aspect ratio of these rods and further slowed down by the phase transformation between $FePO_4$ and $LiFePO_4$ along the rods during the reversible lithiation and delithiation. A recent work, where 3D $LiFePO_4$ nanorods are directly self-aligned on current collectors by using a template, typically exemplified this new challenge.[4] The elongated electronic migration distance and the small contact area between the active species and the main current collector significantly reduce the reaction kinetics of the cell chemistry, which was worsened by the low intrinsic electronic conductivity of $LiFePO_4$. In addition, mechanical stresses induced by lithiation at the interfaces between the nanorods and the current collector could also lead to fracturing upon long-term cycling, adding further barrier to reaction kinetics in these electrodes.

An effective solution to the above issues, which is intrinsic to all rod-like architectures, would be the insertion of an electronically conductive metal-core within the rods, which serves as an intimate electronic pathway between the active species on the stem of the nanorods and the main current collector at the terminal. Such a metal-core would function as a built-in "nano-current collector" that effectively facilitates "electronic transfer", thus accelerating the electrochemistry reaction rate. Since the metal-core is directly rooted onto the main current collector, it can also effectively relieve the stresses of lithiation/delithiation and maintain the integrity of the nanorod, both mechanically and electronically, at high reaction rates and over extended use. Previously, such a metal-core has been fabricated using sacrificed nanostructured templates through a wet impregnation process, followed by etching or template decomposition.[5,6] However, the complexity of that practice and the associated high processing cost would limit its scalability, especially if it is considered as part of the fabrication as MEMS/NEMS power. Hereby we propose a "bottom-up" approach using biological templates to achieve the $LiFePO_4$-nanorods with central metal cores. The genetically modified tobacco mosaic virus (TMV) proves to be a convenient and reliable template that is not only stable but also amenable toward magnetron deposition processes, hence allowing architecturing of sophisticated multilayer energy storage mechanisms.

TMV is a cylindrical high aspect ratio particle, composed of ~2100 identical coat protein subunits assembled onto a positive strand of genomic RNA to produce a nanorod with 300 nm in length, 18 nm in diameter and containing a 4 nm inner channel. Our previous studies have shown that the genetic addition of a cysteine (cys) residue at N-terminus of each coat protein subunit allows for the self-assembly of this engineered virus, TMV1cys, onto metal surfaces through the near covalent-like interaction between the thiol group of the introduced cysteine and the metal atoms. Since this interaction is only possible with the cysteine residues exposed at the end of the cylindrical rod, a nearly vertical assembly of these virus particles ensues, producing a nanoforest of assembled virus templates,[7,8] as shown schematically in Figure 1. More importantly, the presence of cysteine residues enables metal coatings at the virus surface via electroless plating, producing a conductive metal nanoshell around the TMV1cys core. It is important to

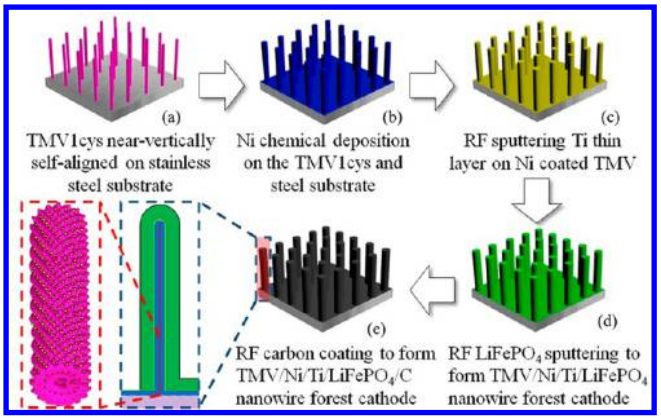

Figure 1. Schematic description of TMV-templated near-vertical assembly of $LiFePO_4$ nanoforest on current collector with multilayered nanohierarchical arrangement of active materials and electron conducting pathway.

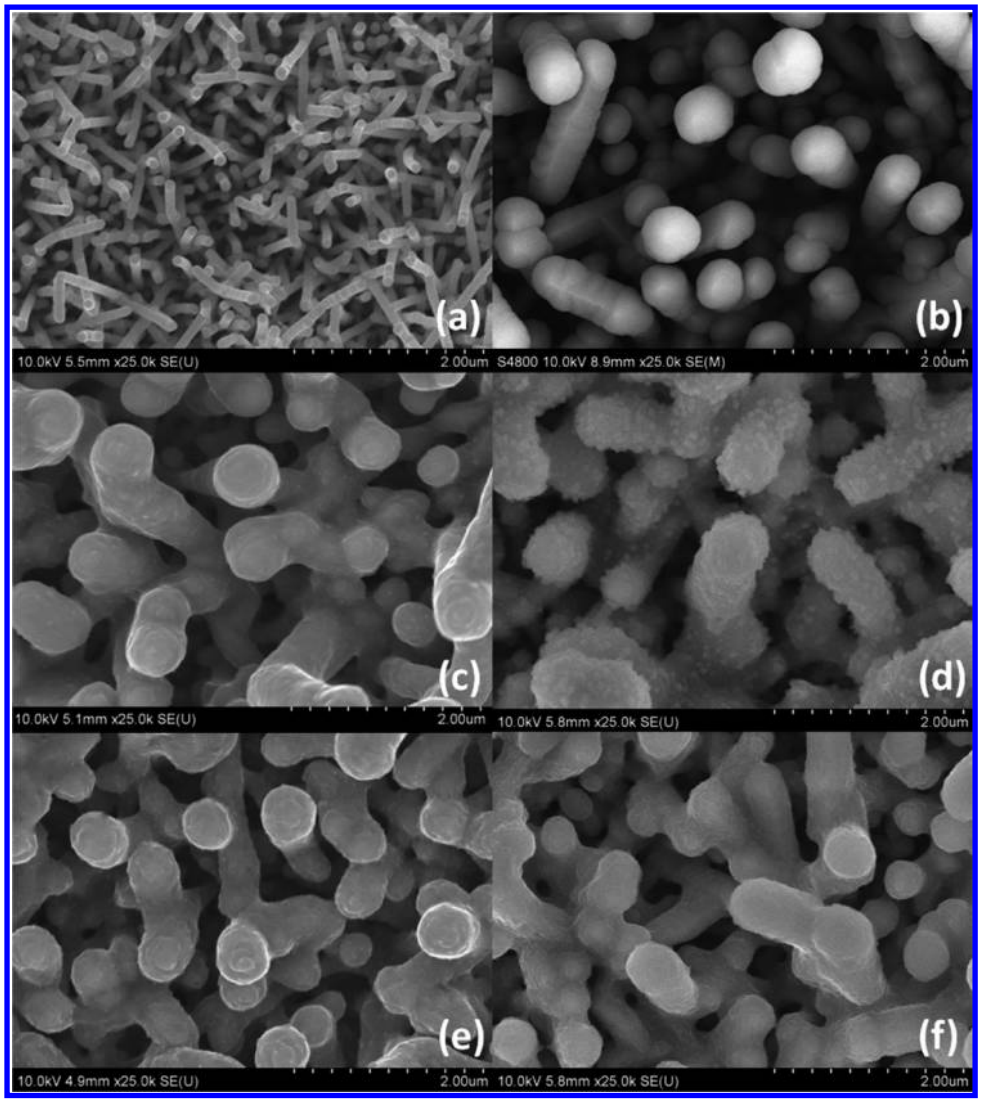

Figure 2. SEM images of the (a) Ti/Ni/TMV1cys on stainless steel, (b) as-deposited $LiFePO_4$/Ti/Ni/TMV1cys, (c) annealed $LiFePO_4$/Ti/Ni nanowire at 500 °C for 2 h, (d) annealed $LiFePO_4$/Ti/Ni nanowire after 450 charge/discharge cycles at a 1 C rate, (e) carbon-coated annealed $LiFePO_4$/Ti/Ni nanowire, and (f) carbon-coated annealed $LiFePO_4$/Ti/Ni nanowire after 450 charge/discharge cycles at a 1 C rate.

emphasize that, differing from the pioneering biotemplate techniques employing engineered M13 bacteriophage templates to biomineralize amorphous a-$FePO_4$ nanowire powders, while the a-$FePO_4$ nanowire cathodes still have to be fabricated through ink-casting of mixture of binder, carbon black and a-$FePO_4$ nanowires,[9,10] the present approach results in a direct assembly and fabrication of 3D nanoforest electrode arrays, which already possess the necessary composite ingredients including a built-in 3D nanocurrent collectors and carbon conductive sublayer but in absence of polymer binder. This unique "bottom-up" can be easily scaled up at low cost or integrated with IC processes.

Thus, as the templates of microelectrode arrays, TMV1cys clones were self-assembled onto a stainless steel (SS) current collector in aqueous solutions (Figure 1a) as described previously, which is sequentially followed by chemical deposition of nickel (Ni) in an electroless plating bath to form a 3D current collector (Figure 1b), radio frequency (RF) magnetron sputtering depositions[11,12] of Titanium (Ti) (Figure 1c) and $LiFePO_4$ sublayers, respectively, to form the multilayered $LiFePO_4$/Ti/Ni/TMV1cys nanoforest (Figure 1d). Eventually, a ~1.65 mg loading mass (1.06 mg/cm^2) of $LiFePO_4$ is obtained, and then the annealing at 500 °C for 1 or 2 h to crystallize the active species. The Ti sublayer between Ni and $LiFePO_4$ is designed for the following purposes: (1) to prevent the electrochemical oxidation of Ni during charging, because the anodic oxidation of Ni occurs near the operating voltage of $LiFePO_4$ (3.5 V vs Li); (2) to alleviate Ni diffusion into $LiFePO_4$ during the high temperature annealing process;[12] (3) to enhance adhesion between $LiFePO_4$ and the "nano-current collectors" as a means to minimize potential capacity loss induced by the mechanical stresses that occurs during electrochemical lithiation/delithiation.

This multilayered composite nanoforest assembly is subsequently coated with an additional sublayer of carbon (C) ~8 nm in thickness (Figure 1e). To electronically wire the outside C coating layer with inner Ni current collector, three small masks in the area of 0.04 cm^2 was placed on 3D Ti/Ni/TMV1cys template before the $LiFePO_4$ deposition. These masks were then removed during the carbon deposition, creating direct pathways between the potential electrochemical reaction fronts and the main current collector.

The above fabrication sequences are individually monitored with scanning electron microscopy (SEM) images. As shown in Figure 2a for the Ni-coated TMV templates, the highly dense forest of Ni/TMV1cys nanorods are arranged on the SS surface in nearly vertical manner, while some TMV1cys self-guide themselves into making longer stacked nanocolumns. The subsequent depositions of Ti and $LiFePO_4$ on these templates forms uniform layers around the rod shaped particles. The final $LiFePO_4$/Ti/Ni/TMV1cys multilayer nanorods have an average of ~500 nm in diameter and >2.5 μm in length (Figure 2b). The thickness of $LiFePO_4$ coating (~200 nm) is 7 times thicker than $LiCoO_2$ layer on Al nanorodes,[13] 12 times of ALD TiO_2 coating on Ni nanorods,[14] and 10 times of $LiFePO_4$ nanorods on Pt.[4]

The as-deposited $LiFePO_4$ nanorods give no apparent diffraction peaks in its X-ray diffraction (XRD) pattern (Figure S1 in the Supporting Information) with an amorphous ring in the FFT figure of the TEM figure (Figure S2a, Supporting Information), indicating its amorphous nature. After heat-treatment at 500 °C for 2 h under vacuum, the smooth surface of the nanorods (Figure 2b) becomes visibly rougher, induced by the phase changes from amorphous to crystalline olivine structure (space group pnma) that occurs during the annealing (Figure 2c) and as evidenced by the XRD patterns in Figures S1 and S2b, Supporting Information. Although the protein-based core of TMV1cys might have been decomposed into inorganic species during this high temperature process, the robust $LiFePO_4$/Ti/Ni shell maintains structural integrity. It should be emphasized here that the virus functions only as a scaffold for the electroless deposition of nickel, therefore its decomposition at the heat-treatment stage no longer impact on the eventual materials performance due to the following reasons. (1) Under the conditions used, we deposited ~10^{-4} g/cm^2 of nickel on the surface of similar virus-assembled electrodes, hence weight contributions from the virus is negligible,[7] and geometrically the thickness of the nickel coatings are nearly twice as that of the virus core. Thus, the virus makes up only a small fraction of the assembled nickel surface. Based on this, we anticipate that carbonization of the virus within the nickel shell would have little if any impact on the nickel structure or its overall make up. (2) On the other hand, we believe that any oxidation of Ni would be unlikely to happen during the process, as carbon-dominated residual of TMV would create a rather reductive atmosphere. In Figure 2e, the carbon-coated $LiFePO_4$ nanorods are shown to have morphology similar to that of the carbon-free $LiFePO_4$ nanorods, with a rather uniform carbon film.

The structure and thickness of each layer in a single $LiFePO_4$/Ti/Ni nanorod after annealing are demonstrated in the transmission electron microscopy (TEM) images and energy dispersive spectroscopy (EDS) element mapping in Figure 3, in which the hierarchy of Ti/Ni metal nanorods of ~80 nm in diameter and the $LiFePO_4$ shell of ~200 nm in thickness are clearly visible (Figure 3a).

Both SEM (Figure 2) and TEM (Figure 3) images cooperatively indicate that within each $LiFePO_4$ nanorod there is a Ti/Ni core that directly connects to the SS main current collector. Thus, the virus-assembled nanoforests carry nearly uniform $LiFePO_4$ coatings (Figure 3a), whose novel multilayered architecture would allow the active shell $LiFePO_4$ to maintain an intimate electrical connection along the entire length of the nanorod during the electrochemical lithiation/delithiation. This intimacy on nanoscale is usually a challenge

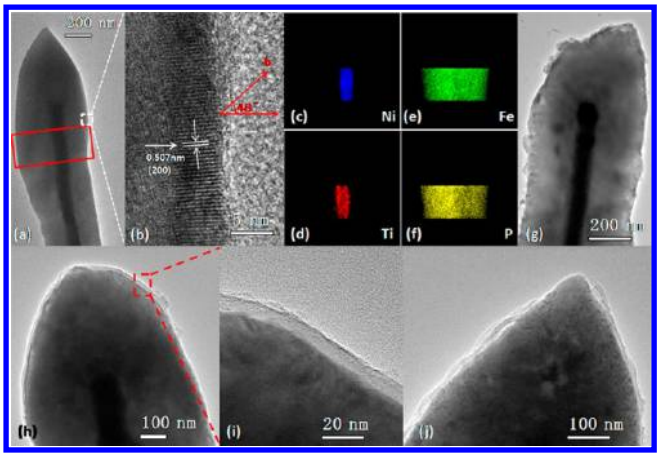

Figure 3. (a) TEM image of $LiFePO_4$/Ti/Ni nanowireafter annealing at 500 °C for 2 h, (b) the high-resolution TEM image of the $LiFePO_4$ crystal. The EDS mapping profiles in the red mapping rectangle were marked in part a for Ni (c), Ti (d), P (e), and Fe (f). Li-ion diffusion channel (*b* axis direction) is marked in part b. (g) TEM image of $LiFePO_4$/Ti/Ni nanowire after 450 cycles at a 1 C rate. TEM image of C/$LiFePO_4$/Ti/Ni nanowire (h) before charge/discharge cycle and (i) and enlarged view of part h and (j) imiage after 450 charge/discharge cycles at a 1 C rate.

for such high aspect ratio configurations and has been the main reason for most degradation of electrochemical performances over long-term cyclings.

The lattice spacing of the $LiFePO_4$ nanocrystal is marked in Figure 3b, which is in accordance with the (200) plane. A selected area diffraction (SAD) analysis (Figure S2b, Supporting Information) was used to calculate the diffusion direction (*b* axis) at the $LiFePO_4$ crystal surface ([1−22]). The small angle of 48° marked in Figure 3b indicates that Li-ions can easily diffuse into $LiFePO_4$ shell from electrolyte since the Li-ion can only transport in *b* axis direction.

A layer-by-layer structural analysis of the annealed $LiFePO_4$ nanowire was further performed by EDS element mapping as shown in Figure 3c−f, which demonstrated that the 10 nm Ti sublayer effectively suppressed the diffusion of the Ni (~50 nm thick) into the $LiFePO_4$ layer (~200 nm), and thus prevents the Ni sublayer from oxidation during charging and minimizes its potential contribution to the irreversible capacity. On the other hand, similar to aluminum (Al), Ti qualifies as an excellent current collector for cathode due to its high stability against oxidation. Therefore the slight diffusion of Ti into both $LiFePO_4$ and Ni sublayers, while enhancing the mechanical stability of the cathode nanorods, does not affect electrochemical stability. Again, consistent with SEM, the decomposition of the TMV1cys inner core during annealing at 500 °C does not lead to any discernible structural disintegration of $LiFePO_4$/Ti/Ni nanorods (Figure 3a). As the interior of the nanoforest electrode arrays, the possible remnants of TMV1cys might consist of largely carbonized amorphous mass doped with heteroatoms (O, N, S, and P etc), which are expected to remain inert during electrochemical reactions. Overall the Ti/Ni nanoshell connected to the SS current collector provides a rather facile electronic transfer pathway across the entire $LiFePO_4$ nanorod; additionally it might also act as a robust backbone that strengthens the mechanical integrity of the electrode arrays upon repeated electrochemical cyclings.

After a single carbon coating, TEM images show that a C sublayer of ~8 nm is uniformly deposited along the $LiFePO_4$/

Ti/Ni composite nanorods. The graphitization degree of the carbon layer can be estimated from the characteristic wide D and G bands in the Raman spectrum at around 1350 and 1600 cm^{-1} (Figure S3, Supporting Information), between which the former (D band) is correlated with structural defects- and disorder-induced features in the graphene layers of carbon materials, while the latter (G band) is indicative of the high-frequency E_2g first-order graphitic crystallites of carbon.[15−17] The presence of the strong D band suggests that the carbon component on the C/$LiFePO_4$/Ti/Ni nanorods have low crystallinity that is typical of disordered graphitic material. No peaks of Fe−O and PO_4^{3-} are detected, confirming that the carbon sublayer fully and uniformly covers the surface of the $LiFePO_4$/Ti/Ni nanoforest.

The electrochemical performance of 3D $LiFePO_4$/Ti/Ni nanoforest cathodes with and without a carbon sublayer were tested in coin cells with typical liquid electrolytes and compared to the performance of reference, a 2D $LiFePO_4$/Ti/SS multilayer thin film cathodes that were deposited under the same conditions but in the absence of the TMV1cys template. The $LiFePO_4$/Ti/Ni nanoforest cathodes have the same active loadings as the 2D $LiFePO_4$/Ti thin film cathodes, but the thickness (∼ 600 nm) of $LiFePO_4$ sublayer in the latter was three times larger than that (∼200 nm) on its 3D counterpart due to inherent high surface area of the former. Figure 4a shows the charge/discharge voltage profiles of two 3D $LiFePO_4$/Ti/Ni nanoforest cathodes, with and without a carbon coating, in comparison with the 2D $LiFePO_4$/Ti thin film cathode at 0.1 C. Both charge and discharge profiles show reversible electrochemical reactions at voltage plateaus around 3.4 V, which is the characteristic phase transition between $FePO_4$ and $LiFePO_4$. The 2D $LiFePO_4$/Ti thin film cathode delivers 78 $\mu Ah/cm^2$, only 53% of its theoretical capacity; in contrast, the TMV-assembled $LiFePO_4$/Ti/Ni nanoforest composite cathodes, containing the same active loading but only 1/3 the thickness of the $LiFePO_4$ thin film cathodes, delivered a discharge capacity of 162 $\mu Ah/cm^2$ (158 mAh/g). Thus the nanoforest architecture produced up to 93% of the $LiFePO_4$ theoretical capacity, obviously benefiting from the shortened distances for both ionic and electronic migration present within the virus template nanorods. Carbon coating on $LiFePO_4$/Ti/Ni nanoforests further enhanced the capacity utilization of active species to 98% of the theoretical value. Among the three cathodes studied, the 3D C/$LiFePO_4$/Ti/Ni nanoforest composite also presents the smallest potential hysteresis between the charge and discharge voltage plateaus, indicating a facile reaction kinetics within this cathode architecture. The flat potential plateau of the carbon coated $LiFePO_4$ nanoforest composite cathode is obviously due to strong Li-polaron coupling that causes Li-ions and electrons to migrate together in an olivine lattice,[18] thus the enhancement of the electronic conductivity by carbon coating also increases the Li-ion mobility while reducing diffusion overpotential during phase change.

TMV1cys enabled 3D $LiFePO_4$/Ti/Ni nanoforest arrays not only enhance the capacity utilization at a low charge/discharge current, but also significantly increase its overall rate performance at higher current densities, which is of particular importance to pulse performances often required in MEMS/NEMS applications, where the capability of electrodes to capture and release energy at fast rates determines efficiency and electrode life. To evaluate the effect of this nano-architecture on fast electrochemical reaction kinetics, the

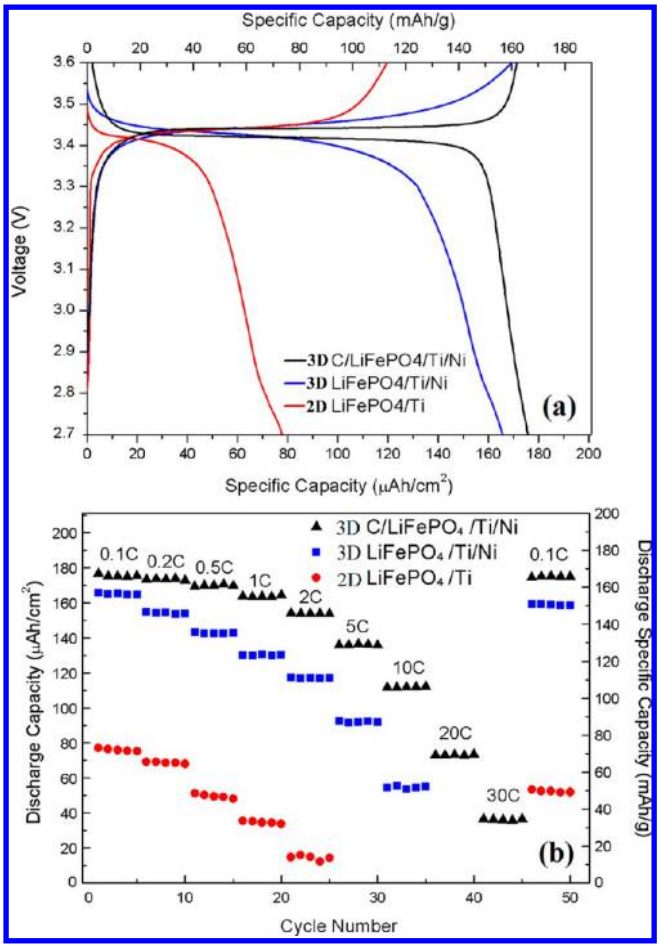

Figure 4. (a) Potential profiles of C/$LiFePO_4$/Ti/Ni, $LiFePO_4$/Ti/Ni nanowire forest cathodes, and $LiFePO_4$/Ti thin film cathode 0.1 C charge/discharge current, and (b) rate performance of 3D C/$LiFePO_4$/Ti/Ni, 3D $LiFePO_4$/Ti/Ni nanowire forest cathodes, and 2D $LiFePO_4$/Ti thin film cathode at different charge/discharge currents.

nanoforest cathodes under investigation were subjected to a rather abusive high rate testing protocol in which the cells were both charged and discharged at the same high rates. As shown in Figure 4b, under this stringent condition, the 2D $LiFePO_4$/Ti thin film cathode can only store and deliver a capacity of 11 $\mu Ah/cm^2$ at 2 C, or 20% of its capacity at 0.1 C, while the 3D C/$LiFePO_4$/Ti/Ni nanoforests with the same $LiFePO_4$ mass loading can deliver as high as 152 $\mu Ah/cm^2$ at the same rate, or 84% of its capacity at 0.1 C. Moreover, the nanoforest cathode with additional carbon coating can deliver 72% of capacity even at 10 C, and 25% at 30 C, respectively. This latter performance of 500 nm C-$LiFePO_4$ nanoforest cathode witnessed a significant improvement in rate performance over 30 nm $LiCoO_2$/Al nanorodes,[13] or 16 nm TiO_2/Ni nanorode electrodes.[14] The rate performance of our C-$LiFePO_4$ is slightly inferior to C-$LiFePO_4$ prepared by Martin's group using polycarbonate filter because the diameter of our C-$LiFePO_4$ is 10 times larger than Martin's C-$LiFePO_4$,[4] and kinetics of $LiFePO_4$ is very sensitive to particle size. With the same $LiFePO_4$ loading per footprint (1.06 mg/cm^2), the 3D C/$LiFePO_4$ forest electrodes provided more 15 times higher capacity than thin film electrode at 2 C. The 3D C/$LiFePO_4$ forest cathode can even be charged and discharged at 30 C, which is not capable for current thin film $LiFePO_4$ electrodes.

To understand the origin of the superior rate performance of the TMV enabled $LiFePO_4$ nanoforest cathode, electrochemical impedance spectra (EIS) were carried out to analyze and compare the reaction resistances of the 3D nanoforest cathodes, both in absence and presence of carbon coatings, as well as the 2D thin film $LiFePO_4$ cathode. In all cases the working cathodes experienced 50 full cycles at a 1 C rate before being charged to 3.6 V at 0.1 C with a subsequent relaxation period of 2 h. Figure 5a shows the Nyquist plots of three

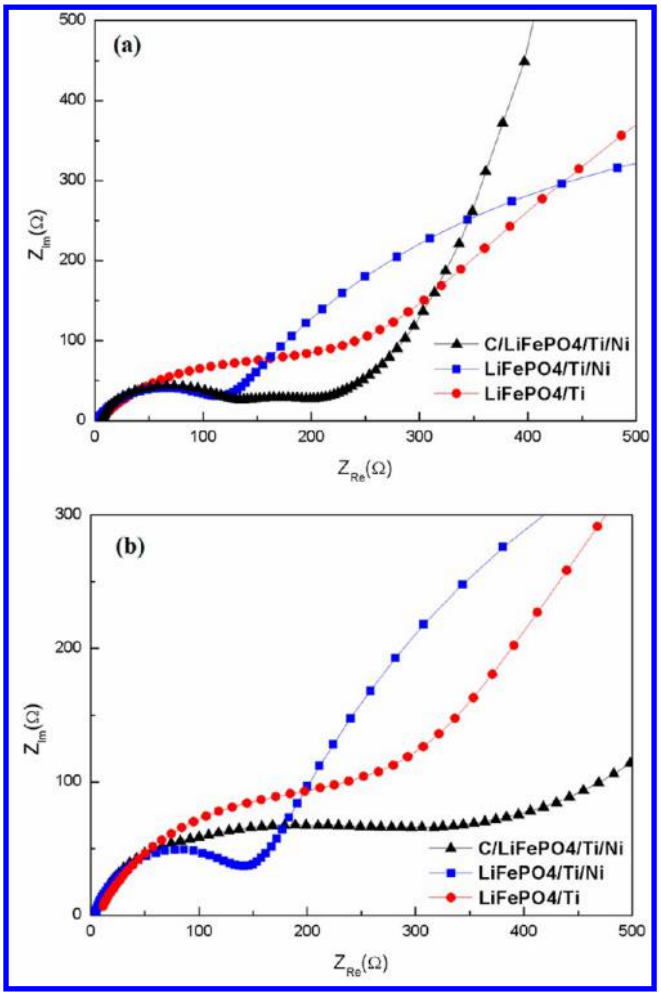

Figure 5. Typical Nyquist plots of three $LiFePO_4$ cathodes (a) after 50 charge/discharge cycles at a 1 C rate and (b) after 450 charge/discharge cycles at a 1 C rate, obtained after charging the $LiFePO_4$ cathode to 3.6 V and relaxation for 2 h.

$LiFePO_4$ cathodes at 50th charge/discharge cycle and Figure 5b is the Nyquist plots of three $LiFePO_4$ cathodes at 450th cycle. For the fully activated $LiFePO_4$ electrodes (Figure 5a), the impedance spectra are typically composed of two partially overlapped semicircles in high and medium frequency regions, and a straight slopping line at low frequency.[19−24] The first semicircle at the high frequency region is attributed to the contact impedance between the current collector and the $LiFePO_4$ active materials,[23,24] while the medium-frequency semicircle corresponds to the charge transfer impedance, which is largely overlapped by the low-frequency Li-ion diffusion line. The Ni nanorod core enhanced the contact between the current collector and the active species $LiFePO_4$ shell, reducing a contact impedance for the nanoforest cathode compared to that of the 2D $LiFePO_4$/Ti thin film cathode. The decreased $LiFePO_4$ thickness as well as low tortuosity paths for ionic transport from the liquid electrolyte into the $LiFePO_4$/Ti/Ni nanoforest cathodes also reduced the lithium-ion diffusion resistance, resulting in a short diffusion tail in low frequency (Figure S4a in Supporting Information) and a short intersection in high frequency (Figure S4b in Supporting Information) in the Nyquist plot, respectively. Further carbon coating on the $LiFePO_4$/Ti/Ni nanorods enhances the charge transfer resistance, reducing the size of the second semicircle and further shortening the low frequency tail (Figure S4a in Supporting Information), an indication that the C sublayer also reduces the lithium-ion diffusion resistance in the $LiFePO_4$ in addition to its assistance in conducting electrons. The combination of these hierarchy elements synergistically leads to the observed superior rate performances of this nanoforest composite cathode.

Finally, in addition to the enhanced reaction kinetics, the nanoforest cathodes also present much improved cycling stability. Figure 6 shows the cycling stability and Coulombic

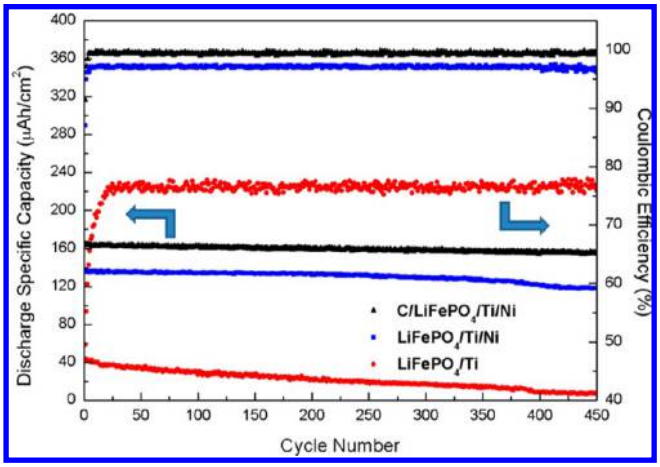

Figure 6. Cycling stability and Coulombic efficiency of $LiFePO_4$ cathodes at a 1 C charge/discharge current.

efficiency of two 3D nanoforest cathodes, C/$LiFePO_4$/Ti/Ni and $LiFePO_4$/Ti/Ni, with the 2D $LiFePO_4$ thin film cathode as comparison. The 3D C/$LiFePO_4$/Ti/Ni nanoforest cathode only decays 0.014% per cycle during cycling at a rate of 1 C for 450 cycles, while the corresponding Coulombic efficiency quickly rises to ∼100% after the first 5 cycles. The 3D nanoforest sample without C sublayer shows a similar cycling stability but with a slightly lower Coulombic efficiency in the first 350 cycles and observable capacity fading thereafter. As comparison, the 2D $LiFePO_4$/Ti thin film cathode without any of the hierarchical nanoarchitecture shows more than 10 times faster capacity decay and low Coulombic efficiency. The low Coulombic efficiency of $LiFePO_4$ thin film electrode in the first few charge/discharge cycles has been reported,[25,26] which has been attributed to the irreversible oxidation of surface impurities such as $Li_xFe_yO_z$, resulting in partial deintegration of iron oxide and ion dissolution into electrolyte. Carbon coating, which presents a far more electrochemical inert surface, can suppress the iron dissolution into electrolyte as evidenced by higher Coulombic efficiency.

As discussed previously, the remarkable cyclic stability of the TMV enabled $LiFePO_4$ nanowire forest cathode could come from the unique multilayer nanohierarchy of the cathode.

Specifically, the highly robust and conductive Ni sublayer strongly binds with active $LiFePO_4$ sublayer through a Ti sublayer and directly connects to the main substrate to form a 3D nanowire extending deeply into the high aspect ratio nanorods. As shown via SEM (Figure 2d) and TEM (Figure 3g), small particles appeared on the surface of the $LiFePO_4$ nanorods but still bonded to the nanorods even after 450 charge/discharge cycles. The carbon coating further improved the morphology and structural stability of 3D $LiFePO_4$ nanoforest cathode. For C/$LiFePO_4$/Ti/Ni nanoforest sample, the surface remains smooth (Figure 2f) after 450 cycles although part of the carbon coating layer is detached from $LiFePO_4$ shell (Figure 3j). These findings indicate that the carbon coating helps in stabilizing the surface morphology of the $LiFePO_4$ layer.

The structural degradation of the $LiFePO_4$ cathodes during charge/discharge cycles would also decrease the kinetics of lithiation/delithiation as demonstrated by EIS (Figure 5b). Comparing EIS at the 50th and 450th cycle in Figure 5, the impedance of all three $LiFePO_4$ cathodes increased with charge/discharge cycles. Both contact impedance (the first semicircle) and charge transfer impedance (the second semicircle) are enlarged after 450 charging/discharging cycles, suggesting the phase transformation generated stress/strains that weakened the bonding between the sublayers of the metal conductor and the active $LiFePO_4$. Phase transformation also induces a change in the morphology of the carbon coating, which increases the charge transfer resistance. The increase in contact resistance and charge transfer resistance in the C/$LiFePO_4$/Ti/Ni nanoforest cathode cause the two semicircles at 50th cycles to merge into a larger one. Thus this hierarchical nanoarchitecture with core−shell arrangements allows the electrode to be charged and discharged at high C-rates with minimized electrochemical and mechanical stresses, resulting in a significant cycling stability improvement over previously reported $LiFePO_4$ nanowire-based cathodes.

It must be pointed out that, while a fully mature application of the process requires both anode and cathode to be architectured in a complementary manner, so that their respective 3D configurations could match each other to make a full battery, we have in our previous work architectured a high capacity 3D anode materials based on Si−Li alloy. Undoubtedly integrating these two electrochemical couples would need further work, but we believe that the current work on 3D $LiFePO_4$ makes one step progress toward that destination.

In summary, an IC-friendly process using genetically modified TMV as "bottom-up" templates leads to $LiFePO_4$-based nanoforest cathode arrays with multilayered hierarchy that functions synergistically to store and deliver energy in small footprint at excellent efficiency and stability. Within the TMV-enabled dense nanoforest cathodes, both ionic and electronic migration lengths are significantly reduced while the mechanical and electrochemical stresses between the intercalation host ($LiFePO_4$) and main current collector are also minimized. The vertical alignment of $LiFePO_4$ nanoforest on SS current collector, enabled by the genetic modification of TMV, and the facile multiple sputtering deposition process provide a valuable new avenue to the 3D electrode array design and architecturing. In particular, the built-in metallic nano-current collector, which significantly enhances the connection between the active sublayer and the main current collector, might provide a versatile solution to the common "electron transfer" issues of high aspect ratio nanostructures.

■ ASSOCIATED CONTENT

Supporting Information

General synthesis and characterization information and figures showing XRD patterns, FFT and SAD images, a Raman spectrum, and Nyquist plots. This material is available free of charge via the Internet at http://pubs.acs.org.

■ AUTHOR INFORMATION

Corresponding Author

*E-mail: (C.W.) cswang@umd.edu; (Y.W.) wyuan@scu.edu.cn; (K.X.) conrad.k.xu.civ@mail.mil.

Notes

The authors declare no competing financial interest.

■ ACKNOWLEDGMENTS

The authors acknowledge financial support from the U.S. Army Research Laboratory and the technical support of the Maryland NanoCenter. We thank Dr. Li-Chung Lai and Fangyu Cao for the TEM and SEM imaging, Yanmei Piao for collecting the Raman data, Jiangwei Wang for indexing the SAD figure. Dr. Yuan Wang would like to acknowledge the financial support from the National Natural Science Foundation of China (Grant No. 51171124) and the Program for New Century Excellent Talents in University (Grant No. NCET-08-0380)

■ REFERENCES

(1) Phan, V. P.; Pecquenard, B.; Cras, F. L. *Adv. Funct. Mater.* **2012**, *22*, 2580−2584.
(2) Long, J. W; Dunn, B.; Rolison, D. R.; White, H. S. *Chem. Rev.* **2004**, *104*, 4463−4492.
(3) Chen, X.; Gerasopoulos, K.; Guo, J.; Brown, A.; Wang, C.; Ghodssi, G.; Culver, J. N. *ACS Nano* **2010**, *4*, 5366−5372.
(4) Sides, C. R.; Croce, F.; Young, V. Y.; Martin, C. R.; Scrosati, B. *Electrochem. Solid-State Lett.* **2005**, *8*, A484−A487.
(5) Qu, J.; Li, H.; Henry, J. J.; Martha, S. K.; Dudney, N. J.; Xu, H.; Chi, M.; Lance, M. J.; Mahurin, S. M.; Besmann, T. M.; Dai, S. J. *Power Sources* **2012**, *198*, 312−317.
(6) Gowd, S. R.; Reddy, A. L. M.; Zhan, X.; Jafry, H. R.; Ajayan, P. M. *Nano Lett* **2012**, *12* (3), 1198−1202.
(7) Royston, E.; Ghosh, A.; Kofinas, P.; Harris, M. T.; Culver, J. N. *Langmuir* **2008**, *24*, 906−912.
(8) Lee, S.; Royston, E.; Culver, J. M.; Harris, M. T. *Nanotechnology* **2005**, *16*, S435−S441.
(9) Lee, Y. J.; Yi, H.; Kim, W.; Kang, K.; Yun, D. S.; Strano, M. S.; Ceder, G.; Belcher, A. M. *Science* **2009**, *324*, 1051−1055.
(10) Lee, Y. J.; Belcher, A. M *J. Mater. Chem.* **2011**, *21*, 1033−1039.
(11) Chiu, K. -F. *J. Electrochem. Soc.* **2007**, *154* (2), A129−A133.
(12) Hong, J.; Wang, C.; Dudney, N. J.; Lance, M. J. *J. Electrochem. Soc.* **2007**, *154* (8), A805−A809.
(13) Shaijumon, M. M.; Perre, E.; Daffos, B.; Taberna, P. -L.; Tarascon, J. -M.; Simon, P. *Adv. Mater.* **2010**, *22*, 4978−4981.
(14) Wang, W.; Tian, M.; Abdulagatov, A.; George, S. M.; Lee, R.; Yang, Y. C. *Nano Lett.* **2012**, *12*, 655−660.
(15) Kim, C.; Park, S.; Cho, J.; Lee, D.; Park, T.; Lee, W. *J. Raman Spectrosc.* **2004**, *35*, 928−933.
(16) Kim, C.; Jeong, Y. I.; Ngoc, B. T. N.; Yang, K. S.; Kojima, M.; Kim, Y. A. *Small* **2007**, *3*, 91−95.
(17) McCann, J. T.; Lim, B.; Ostermann, R.; Rycenga, M.; Marquez, M.; Xia, Y. *Nano Lett* **2007**, *7*, 2470−2474.
(18) Tang, M.; Carter, W. C.; Chiang, Y. -M. *Annu. Rev. Mater. Res.* **2010**, *40*, 501−529.
(19) Pei, B.; Wang, Q.; Zhang, W.; Yang, Z.; Chen, M. *Electrochim. Acta* **2011**, *56*, 5667−5672.
(20) Rui, X. H.; Jin, Y.; Feng, X. Y.; Zhang, L. C.; Chen, C. H. *J. Power Sources* **2011**, *196*, 2109−2114.

(21) Hosono, E.; Wang, Y.; Kida, N.; Enomoto, M.; Kojima, N.; Okubo, M.; Matsuda, H.; Saito, Y.; Kudo, T.; Honma, I.; Zhou, H. *ACS Appl. Mater. Interfaces* **2010**, *1* (1), 212−218.
(22) Min, G. G.; Ko, Y.; Kim, T.-H.; Song, H. -K.; Kim, S. B.; Park, S. M. *J. Electrochem. Soc.* **2011**, *158*, A1267−A1274.
(23) Atebamba, J.-M.; Moskon, J.; Pejovnik, S.; Gabersceka, M. *J. Electrochem. Soc.* **2010**, *157*, A1218−A1228.
(24) Gaberscek, M.; Dominko, R.; Jamnik, J. *J. Power Sources* **2007**, *174*, 944−948.
(25) Zhu, X. J.; Cheng, L. B.; Wang, C. G.; Guo, Z. P.; Zhang, P.; Du, G. D.; Liu, H. K. *J. Phys. Chem. C* **2009**, *113*, 14518−14522.
(26) Song, S.-W.; Reade, R. P.; Kostecki, R.; Striebel, K. A. *J. Electrochem. Soc.* **2006**, *153*, A12−A19.